Hendriyana, A., Bauer, K., Muksin, U., Weber, M. (2018): AIC-based diraction stacking for local earthquake locations at the Sumatran Fault (Indonesia). - *Geophysical Journal International*, *213*, 2, pp. 952—962.

DOI: http://doi.org/10.1093/gji/ggy045

Geophysical Journal International

Geophys. J. Int. (2018) **213,** 952–962
Advance Access publication 2018 February 5
GJI Seismology

doi: 10.1093/gji/ggy045

AIC-based diffraction stacking for local earthquake locations at the Sumatran Fault (Indonesia)

Andri Hendriyana,[1,2] Klaus Bauer,[1] Umar Muksin[3] and Michael Weber[1,4]

[1]*German Research Centre for Geosciences GFZ, Potsdam, D-*14473 *Potsdam, Germany. E-mail: hendriyana@gf.itb.ac.id*
[2]*Faculty of Mining and Petroleum Engineering, Bandung Institute of Technology (ITB),* 40132 *Bandung, Indonesia*
[3]*Tsunami and Disaster Mitigation Research Center, Syiah Kuala University, Banda Aceh, Indonesia*
[4]*Institute of Earth and Environmental Science, University of Potsdam, D-*14476 *Potsdam, Germany*

Accepted 2018 February 2. Received 2018 January 3; in original form 2017 May 2

SUMMARY

We present a new workflow for the localization of seismic events which is based on a diffraction stacking approach. In order to address the effects from complex source radiation patterns, we suggest to compute diffraction stacking from a characteristic function (CF) instead of stacking the original waveform data. A new CF, which is called in the following mAIC (modified from Akaike Information Criterion) is proposed. We demonstrate that both *P*- and *S*-wave onsets can be detected accurately. To avoid cross-talk between *P* and *S* waves due to inaccurate velocity models, we separate the *P* and *S* waves from the mAIC function by making use of polarization attributes. Then, the final image function is represented by the largest eigenvalue as a result of the covariance analysis between *P*- and *S*-image functions. Results from synthetic experiments show that the proposed diffraction stacking provides reliable results. The workflow of the diffraction stacking method was finally applied to local earthquake data from Sumatra, Indonesia. Recordings from a temporary network of 42 stations deployed for nine months around the Tarutung pull-apart basin were analysed. The seismic event locations resulting from the diffraction stacking method align along a segment of the Sumatran Fault. A more complex distribution of seismicity is imaged within and around the Tarutung basin. Two lineaments striking N-S were found in the centre of the Tarutung basin which support independent results from structural geology.

Key words: Time-series analysis; Body waves; Computational seismology; Earthquake source observations; Seismicity and tectonics.

1 INTRODUCTION

The classical method of seismic event localization is based on the picking of body wave arrivals, ray tracing and inversion of traveltime data. Traveltime picks with small uncertainties are required to produce reliable and accurate results with this kind of source localization. Hence, recordings with a low signal-to-noise ratio (SNR) cannot be used in a traveltime-based inversion. Diffraction stacking is considered as an alternative seismic event localization method that enables the processing of low SNR recordings by mean of stacking the amplitudes of seismograms along a traveltime function. The location of seismic event and its origin time are determined based on the highest coherence (i.e. stacked amplitudes) of the image function. The method promotes an automatic processing since it does not require traveltime picks as input data.

The influence of the earthquake source radiation pattern on the signals to be stacked has to be considered in the diffraction stacking of passive seismic data. In seismic reflection data, for which the diffraction stacking was developed, the signals to be stacked are generated by approximately isotropic sources such as hammer, explosions or vibroseis. After application of different processing steps such as static corrections and amplitude corrections, the signals are rather comparable and can be stacked by simple mean or other statistical methods. In passive earthquake seismic recordings, a much more complex source mechanism has to be assumed. The double-couple (DC) source model is an approximation model representing the actual radiation by an earthquake source. In addition, some seismic events have a significant amount of non-DC component, if the fault plane is not planar. The non-DC component can be found, for example in seismic events recorded in a volcanic area (Julian 1983). A source model for passive seismicity may be well represented by a mixture of isotropic component, DC component and compensated linear vector dipole component (Vavryčuk 2015), which further leads to the variation of phase polarities and amplitudes at the onsets of *P* and *S* waves at different stations. In such cases, the stacked amplitude computed from the recorded seismogram will be low (Staněk *et al.* 2015). In a pure DC source model, the resultant stacking amplitude may be zero, caused by the cancelation of positive and negative polarities (Zhebel 2013). Numerous techniques of computing coherence which consider the source

radiation pattern of passive seismic data have been suggested, such as pairwise cross-correlation (Zhebel 2013). Anikiev *et al.* (2014) conducted automatic moment tensor inversion prior to stacking the amplitudes; hence the stacking was applied to the corrected polarity onset of the *P* wave. Avoiding low coherence values can also be achieved by transforming the seismogram amplitudes to a characteristic function (CF). Kao & Shan (2007) employed stacking to the absolute amplitude of seismogram. An envelope of amplitudes was also used by Kao & Shan (2007) and Gharti *et al.* (2010). Other CFs were also proposed to highlight the onset of *P* or *S* waves such as short-term average amplitude to long-term average amplitude ratio (STA/LTA, Grigoli *et al.* 2013, 2014; Pesicek *et al.* 2014; Hansen & Schmandt 2015) and differential kurtosis (Langet *et al.* 2014).

The effect of different CFs calculated for a local earthquake recording is shown in Fig. 1. The manually picked arrival times of *P* and *S* waves are indicated by grey lines. The STA/LTA response (Fig. 1d) was computed by an approach suggested by Withers *et al.* (1998). The short and long window length are 0.2 and 1 s, respectively (the dominant period of the signal is about 0.1 s). The STA/LTA was derived from signal envelope (Fig. 1c). The kurtosis CF (Fig. 1e) was calculated by using a window length of 1 s. The Akaike Information Criterion (AIC) function (Fig. 1f) was computed as expressed by eq. (1). Since diffraction stacking localization makes use of amplitude variations around the *P* and *S* onsets, it is obvious that the original waveform (Fig. 1a), the absolute amplitude (Fig. 1b) and the envelope (Fig. 1c) are not well suited for the application of the diffraction stacking method. The STA/LTA and kurtosis show two peaks at the location nearby the onset of *P* and *S* waves. However, the two peaks do not coincide very well with the estimated seismic wave onsets particularly at the *S*-wave onset. On the other hand, it can be seen that the minimum of AIC function coincides well with the estimated *P*-wave onset. Hence, an AIC-based CF was designed and used in this study to exploit its potential in diffraction stacking of local earthquake data.

In this paper, we further study the opportunity of using AIC (Maeda 1985) as a CF for event localization. AIC was used as a tool to accurately estimate the onset of *P* and *S* waves arrival times (e.g. Jousset *et al.* 2011). However, its usage depends on a window length of the seismogram. To be precise, only one single onset of seismic phase is allowed within the window. We, thus, develop a modified AIC (mAIC) by computing the AIC in a translatable window that allow us to analyse a continuous seismogram, regardless how long the window size and how many seismic phases are recorded within a window. The results show that the mAIC effectively identifies various seismic phases, including onsets of *P* and *S* waves. Furthermore, to improve the accuracy of seismic event locations, amplitude stacking is computed from both *P* and *S* waves.

In order to image the location of seismic event, Gharti *et al.* (2010) conducted the diffraction stacking simultaneously from seismograms in the LTQ coordinate system. The *P*-velocity model was used to compute the coherence of *L*-component seismograms, while the coherence of the *T* and *Q* components were computed using the *S*-velocity model. The final image was a result of summing up the coherence of the three components LTQ of the seismograms. In another approach, Grigoli *et al.* (2013) suggested to construct the image function separately derived from *P* and *S* CFs. The final image is derived in this case by multiplication of the *P*- and *S*-image functions. Transforming the seismogram into the ray coordinates, LTQ requires knowledge of the backazimuth and incident angle. These two angles should be computed for each gridpoint as they are potential source locations. If the computed angles contain large uncertainties (caused by noise or complex velocities), the separation

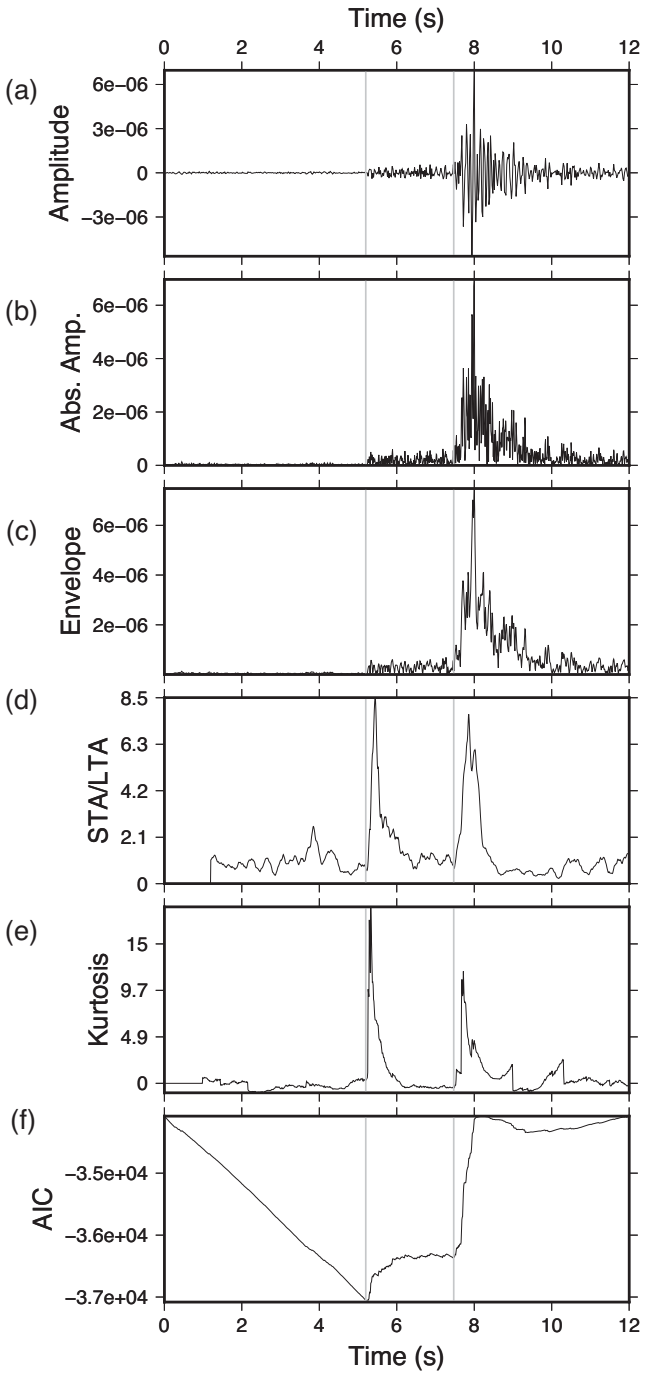

Figure 1. (a) Local earthquake seismogram and its characteristic functions consist of (b) absolute amplitude, (c) envelope, (d) STA/LTA, (e) kurtosis and (f) AIC.

of *P, SV* and *SH* would not be optimal. In our proposed method, the *P* and *S* waves were treated separately in computing the diffraction stacking. The final image was obtained from the covariance analysis of the *P*- and *S*-image functions. The phases of *P* and *S* waves were derived from the mAIC CF in combination with attributes from polarization analysis that is the largest eigenvalue. In order to evaluate its performance, the proposed localization approach was applied to synthetic seismograms and real data recorded at the Tarutung region, Sumatra-Indonesia.

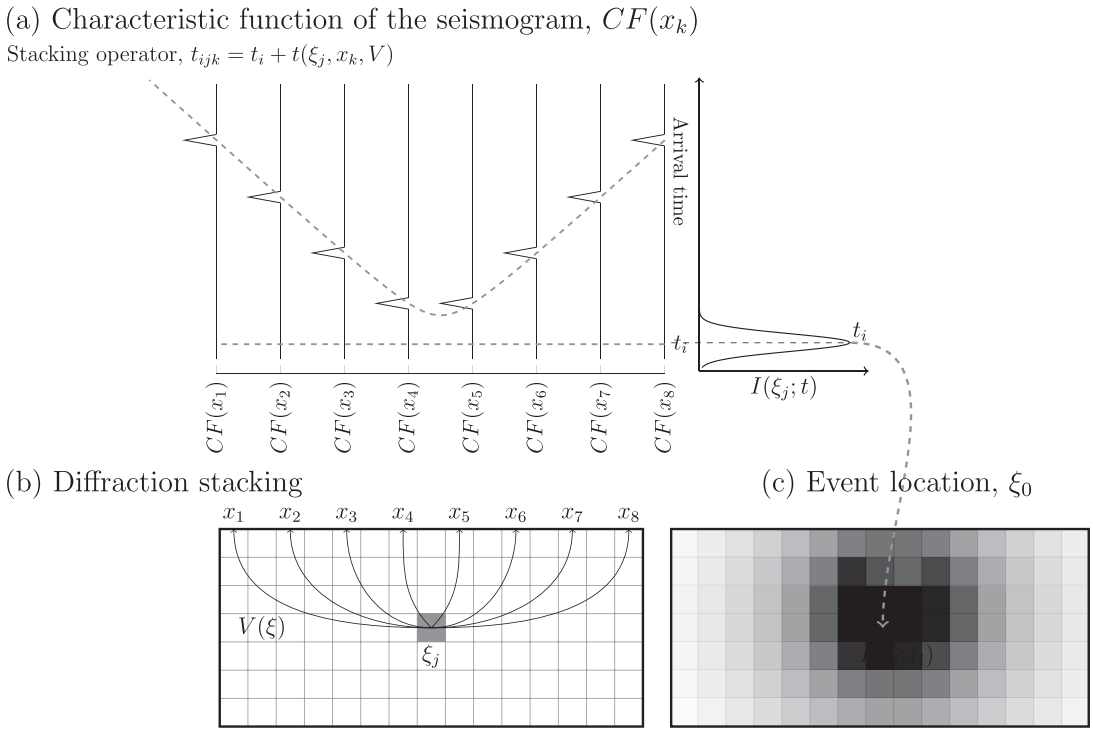

Figure 2. Illustration of the seismic event localization using the diffraction stacking method. (a) The characteristic function is calculated from the raw seismogram. (b) The image function of a particular nodal point ξ_j is estimated by use of diffraction stacking. The diffraction stacking is applied to both *P* and *S* characteristic functions independently using the corresponding stacking operator derived from the *P*- and *S*-wave velocity models, $V(\xi)$. (c) The seismic event, ξ_0, is estimated from the probability density function of the image function $I(\xi)$.

2 METHODS

The diffraction stacking seismic event localization is accomplished in three steps (Fig. 2). In the first step, pre-processing procedures are applied to the raw seismogram such as bandpass filtering and transformation into the mAIC CF. The second step is computing the image function by applying amplitude stacking of the CF along a stacking operator that is computed based on the *P*- and *S*-velocity models. In the third step, by following Anikiev *et al.* (2014) the seismic event and its uncertainty are determined from the probability density function that is derived from the final image function. One of the advantages of using this approach in estimating event location is that the located event is not restricted by the grid spacing. It is not necessary that the location of seismic event should be in the nodal point. Each of these three steps are explained in more detailed in the following.

2.1 Modified AIC characteristic functions

For a discrete seismogram $s = \{s_1, s_2, \ldots, s_N\}$ with N samples, the AIC of the seismogram is defined as (Maeda 1985),

$$\mathrm{AIC}(j)_{1,N} = j \log \mathrm{var}[s(1:j)] + (N-j-1) \log \mathrm{var}[s(j+1:N)], \quad (1)$$

where the subscript in $\mathrm{AIC}(j)_{1,N}$ means that the AIC function is computed from the first sample until the *N*th sample of a seismogram. *j* runs through all of the samples of a seismogram. log is a natural logarithm and var is the variance of the seismogram amplitudes.

The mAIC function is determined by use of a moving time window with a fixed length. The mAIC value of a specific sample is calculated within the moving time window. The window length is set much smaller than the length of the seismogram (i.e. 0.5 s). The classical AIC computation (eq. 1) is used in each window, and the mAIC value is obtained by measuring the distance from the AIC value to its maximum value at a specified point. The mAIC is expressed as:

$$\mathrm{mAIC}(k) = \max\left\{\mathrm{AIC}(j)_{k-n_1,k+n_2}\right\} - \mathrm{AIC}(k)_{k-n_1,k+n_2}. \quad (2)$$

The time index *k* runs from 1 to *N* whereas *j* runs from $k - n_1$ to $k + n_2$. n_1 and n_2 are the number of samples before and after the sample *k* being analysed. The total length of the calculation window, $n_1 + n_2$, is supposed to be smaller than the delay time between *P*- and *S*-wave onsets, thus, the *P* and *S* waves could be well detected by the mAIC CF. The comparison of AIC and mAIC of a seismogram containing two seismic events is shown in Fig. 3. The AIC is computed using one time window from 0 until 35 s; whereas the mAIC is calculated using a translatable window of 1 s with n_1 equals n_2. The global minimum of the AIC function only corresponds to the *P* wave arriving at around 5 s (Fig. 3b). The *S* wave which is following this *P* wave cannot be identified easily from the AIC function. The AIC function at the time in which the second seismic event is occurring does not indicate any (local) minimum. On the other hand, the *P* and *S* onsets from the two seismic events can be easily detected in the mAIC CF.

Fig. 4(b) shows an example of the mAIC computed from the raw seismogram shown in Fig. 4(a). The mAIC functions are calculated from each component of the recorded seismogram using 0.4 s window size. The form of the mAIC functions highlights the *P*- and *S*-wave onsets. At this example, both mAICs resulting from both horizontal seismograms also indicate the *S* wave.

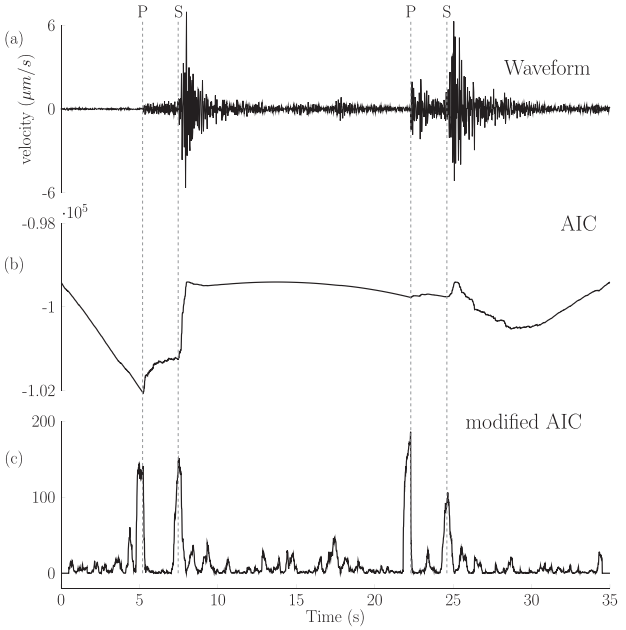

Figure 3. The modified AIC function. (a) Raw seismogram containing two seismic events. Each seismic event is indicated by *P*- and *S*-wave onsets. (b) The AIC function generated from the raw seismogram using eq. (1). (c) The modified AIC characteristic function that was calculated with eq. (2) using a window with 1 s length. The onsets of the *P* and *S* waves determined manually are indicated by dashed lines.

2.2 Separating the *P* and *S* characteristic functions

In order to minimize the cross-talk between *P* and *S* CF during the amplitude stacking due to inaccurate velocity models, we separate the *P* and *S* CFs from the mAIC CFs. To extract the *P* and *S* CFs (CF^p and CF^s, respectively) from the mAIC function, we make use of the largest eigenvalues that are derived from the covariance analysis of the three-component seismograms. The use of the largest eigenvalue to indicate the *S* phase has been proposed by Grigoli *et al.* (2014). To compute the largest eigenvalue, we first compute the covariance matrix, $C(t)$, that is,

$$\mathbf{C}(t_i) = \begin{bmatrix} \mathrm{var}(Z) & \mathrm{cov}(Z,N) & \mathrm{cov}(Z,E) \\ \mathrm{cov}(N,Z) & \mathrm{var}(N) & \mathrm{cov}(N,E) \\ \mathrm{cov}(E,Z) & \mathrm{cov}(E,N) & \mathrm{var}(E) \end{bmatrix}, \quad (3)$$

with $Z(t)$, $N(t)$ and $E(t)$ denote the particle motion as functions of time. The calculation of the covariance matrix is conducted in a time window with *M* samples, and one element of the covariance matrix can be expressed by:

$$\mathrm{cov}(A_i, B_i) = \sum_{t=i-M/2}^{t=i+M/2} (A_t - \overline{A})(B_t - \overline{B}), \quad (4)$$

where $\overline{A}$ and $\overline{B}$ are the mean of particle motions recorded at components *A* and *B* computed within a selected time window with the size of *M* samples. The resulting covariance value is assigned to the centre of the moving window. Three eigenvalues ($\lambda_1 \geq \lambda_2 \geq \lambda_3$) are computed from the covariance matrix (eq. 3). This eigenvector has a physical meaning as the vector of propagation of particle motion, whereas the eigenvalues represent the radii of the best-fitting ellipsoid. One example of the largest eigenvalue function calculated from a raw seismogram is presented in Fig. 4(c). Since the amplitudes of the *S* wave are larger than that of the *P* wave, the maximum value of the largest eigenvalue function coincides with the *S* wave.

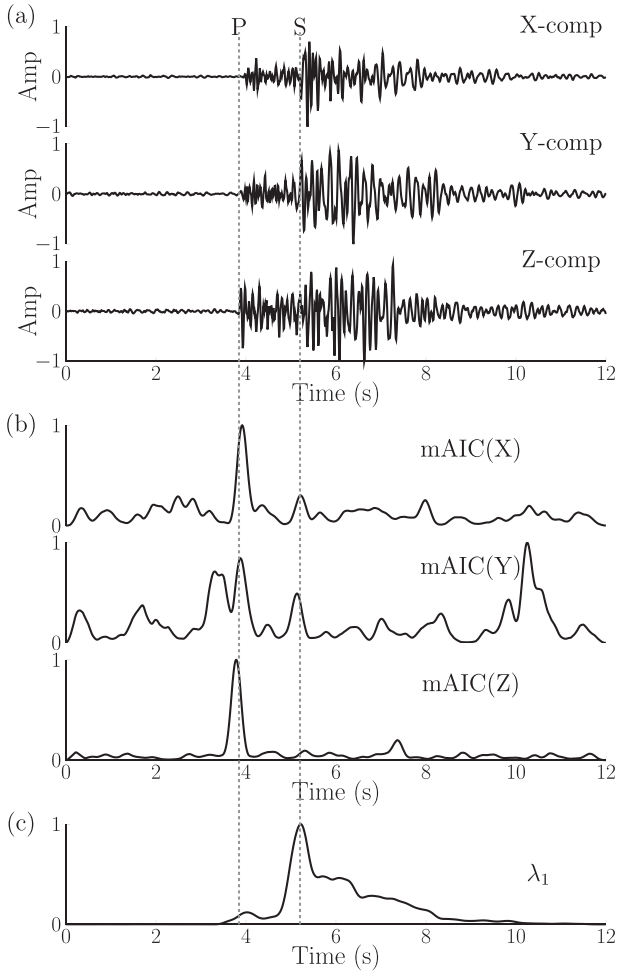

Figure 4. The mAIC characteristic functions of the three-component seismograms. (a) Raw seismic recorded at station ST27 (see Fig. 8) related with seismic event occurred on 2011 August 8. (b) The corresponding mAIC function for each component calculated using a window length of 0.4 s. (c) The largest eigenvalue resulting from applying covariance analysis using 0.4 window size. The manually estimated *P*- and *S*-wave onsets are indicated by grey lines.

After the largest eigenvalue has been estimated, the *S* CF is obtained by multiplying the mAIC function of the horizontal component with the largest eigenvalue λ_1. This would be:

$$\mathrm{CF}_c^s = \left[\mathrm{mAIC}(c)\lambda_1^2\right] \quad \text{with} \quad c = N, E. \quad (5)$$

To reduce noise, the final *S* CF is estimated from the combination of the WE and SN components, as described by:

$$\mathrm{CF}^s = \left[\mathrm{CF}_N^s \times \mathrm{CF}_E^s\right]. \quad (6)$$

Please note that the final *S* CF is estimated only from the two horizontal components of a seismogram.

The *P*-phase CF of a specific seismogram component *c*, is defined as:

$$\mathrm{CF}_c^p = \mathrm{mAIC}(c) \quad c = Z, N, E. \quad (7)$$

The *P*-phase CF, unlike the *S* CF, is determined by combining the three components of the seismogram, as represented by eq. (8).

$$\mathrm{CF}^p = \left[\mathrm{CF}_Z^p \times \mathrm{CF}_Z^p \times \mathrm{CF}_N^p \times \mathrm{CF}_E^p\right]. \quad (8)$$

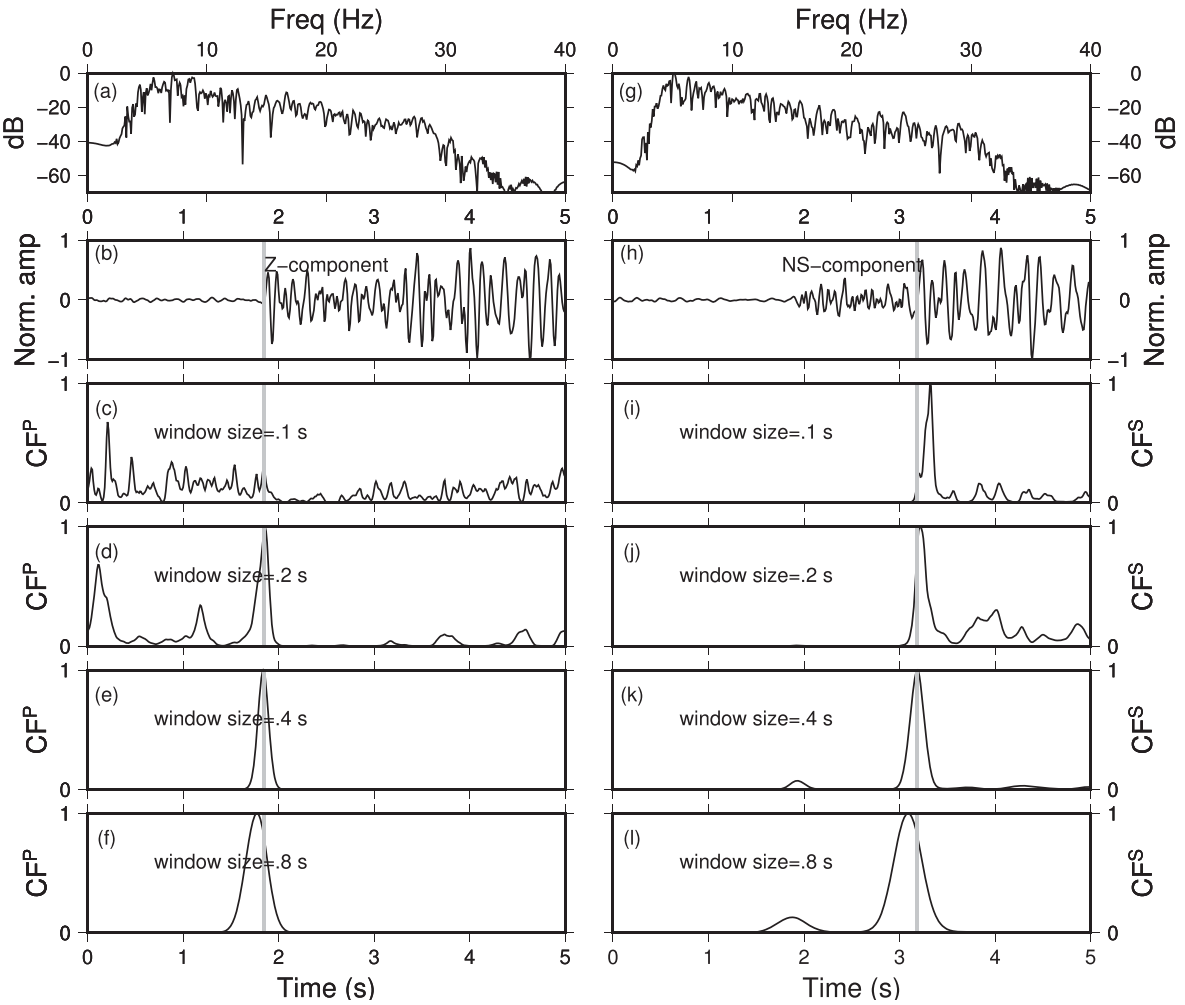

Figure 5. (c)–(f) *P* and (i)–(l) *S* characteristic functions resulting from the application of eqs (8) and 6 to (b) and (c) three-component seismogram with different size of moving window. The window size of (c) and (i) 0.1 s, (d) and (j) 0.2 s, (e) and (k) 0.4 s and (f) and (l) 0.8 s are used. The location of *P*- and *S*-wave onsets estimated by manual are shown in grey lines. The dominant signal period of 0.1 s was assumed after examining (a) and (b) the frequency spectra.

In order to find an optimal window size for computing mAIC CF, we consider the frequency of the signal. The frequency spectra of the recorded seismogram (Figs 5b and h) are shown in Figs 5(a) and (g). The dominant frequency of this seismogram is about 10 Hz. By considering the dominant period of 0.1 s, different window sizes such as 0.1, 0.2, 0.4 and 0.8 s have been chosen to examine a proper length of the moving window. These sizes of window have also been used for polarization analysis and triangular smoothing (Claerbout & Fomel 2014). For example, 0.1 s was used as window size for polarization analysis, triangular smoothing and mAIC calculation. The *P* and *S* CFs of the recorded seismogram using window size of 0.1, 0.2, 0.4 and 0.8 s are shown in Figs 5(b)–(f) and Figs 5(h)–(l). The longer the size of the moving window, the larger the shifting of the peak of the CF with respect to the estimated wave onset, particularly for the *S*-wave onset. However, choosing the smallest window size is also not an appropriate choice, since it will make the mAIC more sensitive to coda waves as indicated by Fig. 5(c). Best results are obtained if the window length equals to twice of the dominant period. The peak of the *P* and *S* CFs coincide with the time of the *P*- and *S*-wave arrivals, then it is expected that utilizing these functions as input for the diffraction stacking localization would lead to a better seismic event location, rather than using the original, recorded waveform.

2.3 Diffraction stacking

In the second step, we apply the diffraction stacking into the *P* and *S* CFs (Figs 2 a and b). The diffraction stacking localization method is a grid search approach. A number of test models are considered as candidates for the location and origin time of a seismic event, and the objective function (also referred to as the coherence function) is evaluated for each possible test model. The highest coherence is sought, since it is associated with the event location (Grigoli *et al.* 2014). The test models are represented by spatial and temporal informations of a seismic event. The test models can be provided by discretizing the subsurface (spatial) and time (temporal) regularly in a fixed grid size. *A priori* information can be introduced to constrain the spatial and temporal model space. The coherence at each grid, in this model, is measured along the traveltime function which is called the stacking operator. The traveltime is constructed based on the assumed *P*- and *S*-velocity models obtained from previous studies.

In this study, we apply diffraction stacking by adopting the approaches of Gajewski *et al.* (2007) and Langet *et al.* (2014). First, the subsurface model is discretized and each nodal point (ξ_j) is assumed as a potential location of a seismic event (Fig. 2b). The traveltimes from each nodal point of the model to each surface station are calculated using the assumed *P*- and *S*-velocity models

(Fig. 2a). After choosing a time t_i for a guest origin time, the function of stacking operator, t_{ijk}, can be built by $t_i + t_{jk}$. t_{jk} is a traveltime from the gridpoint ξ_j to the station k. The image function (or objective function) is composed by collecting the stacked amplitude of P and S CFs, CF^l, correspond to all discretized models (t_i and ξ_j):

$$I^l(\xi_j; t_i) = \sum_{t_w=-T/2}^{+T/2} \sum_{k=1}^{M} \mathrm{CF}^l \left[t - (t_{ijk} + t_w); \xi_j \right], \tag{9}$$

$l = P$, S and M is number of seismometer stations in a network. The amplitude stacking is performed within a time window with a length of T samples. The length of time window used for computing the P and S CFs, which considers the dominant period of signal, can be considered as a proper choice for the length of stacking window. The stacking was applied to the P and S CFs independently by using the P- and S-velocity models. Finally, the P- and S-image functions, I^P and I^S, are obtained. I^P and I^S are 4-D image functions. However, we do not store the 4-D image functions. At a gridpoint ξ_j, we look at the function $I(\xi_j; t)$, then we only store $I(\xi_j; t_i)$ in which t_i is the time associated with the peak or the maximum value of the image function $I(\xi_j; t)$ (see Fig. 2):

$$I(\xi_j) = I(\xi_j; t_i). \tag{10}$$

Here, we proposed to reconcile the P- and S-image functions by employing the covariance analysis. The covariance matrix is computed at each gridpoint ξ_j by involving n points surrounding the location being investigated. The covariance matrix between the P- and S-image functions can be expressed by:

$$\mathrm{cov}(I^p, I^s) = \begin{pmatrix} I^{pp} & I^{ps} \\ I^{ps} & I^{ss} \end{pmatrix}. \tag{11}$$

The largest eigenvalue of the covariance matrix is chosen to represent the final image function.

The third step is determining the seismic event location from the final image function (Fig. 2c), instead from the P or S diffraction image function. The final image function is represented by the value resulting from the covariance analysis between the P and S diffraction images as described by eq. (11). In the maximum approach, the uncertainty of the located event is limited by the grid spacing. Then, to improve the accuracy, we estimate the event location by transforming the final image to its probability density function. Following the method suggested by Anikiev *et al.* (2014), we determine the location of seismic event and its uncertainty.

The quality of velocity model would affect the image of diffraction stacking. An accurate velocity model leads to a focused image. Whereas an inaccurate one would produce diffuse or scattered image of diffraction stacking. Besides the location of seismic event, the location uncertainty (standard deviation) can be extracted from the probability density function. The imperfect velocity model would clearly lead to large uncertainty and a large uncertainty corresponds to a diffuse diffraction image function.

3 SYNTHETIC TEST

To evaluate the proposed method, we apply our localization method to synthetic data sets generated by a source occurring at a known location ($x = 12.5$ km, $y = 12.5$ km and $z = 7$ km) (Fig. 6). The 3-D model consists of two layers with P-wave velocities of 2 and 3 km s^{-1}, respectively. The S-wave model was obtained by dividing the P-wave model with $\sqrt{3}$. The source is located in the second layer. In order to avoid the reflection from the interface between these two layers, then the velocity models were smoothed using

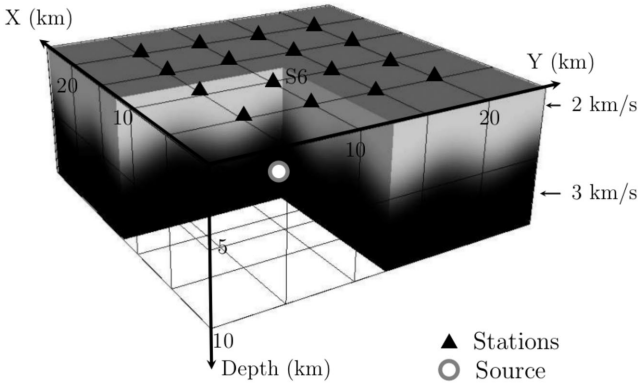

Figure 6. Synthetic geological model used consisting of two layers, each with velocities of 2 and 3 km s^{-1}, respectively. 16 seismometers are deployed at a depth of 100 m at the positions indicated by triangles.

triangular smoothing (Claerbout & Fomel 2014) with a smoothing radius of 2 km to produce smooth interface between different layers. The seismic waves from the source were registered by 16 three-component seismometers (black triangles in Fig. 6) installed at a depth of 100 m. Their sampling rate and recording length are 2 ms and 14 s, respectively. The source mechanism is associated with a left-lateral strike slip in the direction of N 90^o E with a half-duration of 0.1 s. The synthetic seismograms were modelled using the SPECFEM3D program (Tromp *et al.* 2008). A simulation of wave propagation from one source was accomplished on 324 processors within approximately 5 min at the GFZ computing centre.

In our method, the original seismograms have to be transformed into the mAIC CF. The mAIC functions were computed for each component (X,Y and Z) using a 0.25 s window length. Please note that to compute the mAIC CF, it would be better to normalize the amplitudes of seismograms to avoid very small amplitude values (since particle velocity seismograms are used). To obtain the P CF, the mAIC functions from all three components were combined using eq. (8). To estimate the S CF, the mAIC from the horizontal components were combined with the largest eigenvalue (eq. 5). The polarization analysis to estimate the largest eigenvalue was conducted using a 0.25 s window length.

As the traveltime database has to be considered at all gridpoints as sources, preparing this database takes a significant amount of time. To minimize this computation time, we apply the reciprocity principle, thus, traveltimes were calculated by considering seismometers, rather than gridpoints, as source locations. The model has a size of 25 km × 25 km × 10 km (Fig. 6) and it is discretized at 100 m spacings. The traveltime database can be used to localize any seismic event which is located within the network.

The amplitude of the P and S CFs are stacked along the traveltime function that are built from the exact P- and S-wave velocity model, respectively. This means that the event localization and synthetic seismogram modeling used the same velocity model. From the P CF and P-wave velocity model, we reconstruct the P-image function. The S-image function is resulted from the use of S CF and S-wave velocity model. The interpretation of the seismic event location is conducted in the PS-image function as described by eq. (11). The amplitude stacking was calculated by applying diffraction stacking using a 0.2 s window length. In this synthetic example, we apply amplitude stacking to synthetic seismograms and the corresponding CFs with the aim to compare the resulted image functions. Fig. 7 compares these image functions. The PS image resulting from

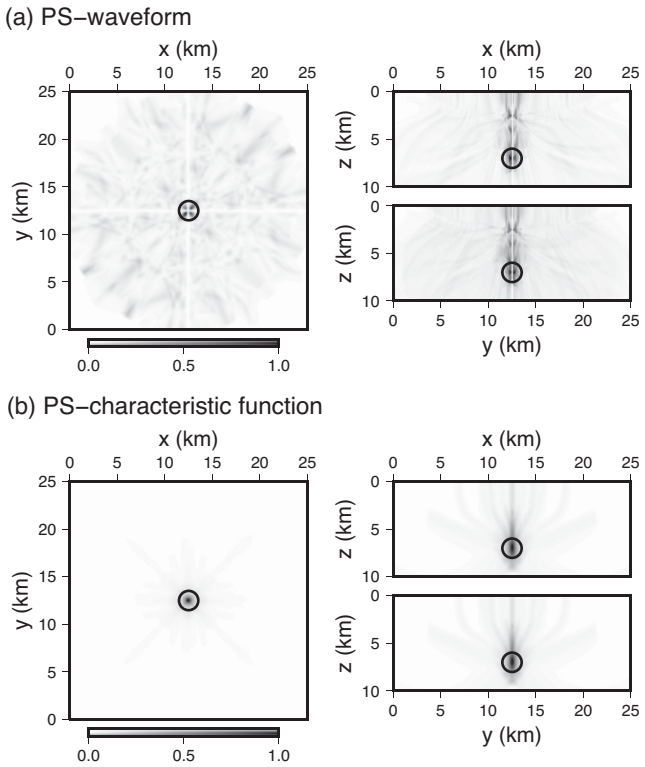

Figure 7. Slice of the *PS*-image functions through the exact location of the seismic event ($x = 12.5$ km, $y = 12.5$ km and $z = 7.0$ km) as indicated by the black circle. (a) The *PS*-image function was resulted from the application of the diffraction stacking to the seismograms and (b) the *PS*-image function was calculated from the characteristic functions.

the waveform stacking of original waveforms shows a complicated image at the location of a seismic event (black circle) since the DC source model was used. The cancelation of amplitudes is seen at the exact location of the seismic event. Whereas the *PS* image resulting from the stacking of the CF presents a focusing image. The maximum image value can be easily estimated from the coalesced image function which is at the position ($x = 12.5$ km, $y = 12.5$ km and $z = 6.9$ km). The maximum of image function can be associated with the looked for source location. Then, the calculated source location resulting from this *PS*-image functions are located at the exact seismic event location at point ($x = 12.5$ km and $y = 12.5$ km). The depth location estimated from the *PS*-image functions is 6.9 km. The estimated depth is underestimated by 100 m (one grid node) from the true location.

4 TARUTUNG LOCAL EARTHQUAKE DATA

Passive seismic monitoring at the Tarutung and Sarulla regions were conducted from 2011 May to 2012 February (Muksin *et al.* 2013). The purpose of this experiment was to study the role of fault structures on the geothermal setting inside this region. The deployment included 40 seismic stations equipped with short-period Mark sensors (1 Hz), and two stations with Broadband sensor 3C PE-6/B4.5 Hertz. Digital seismograms were registered using PR6-24 Earth Data Logger (for short-period sensors) and DSS Cube Data Loggers, Omnirecs (for Broadband sensors). A temporal sampling rate of 100 Hz was used. Most of the seismometers were installed

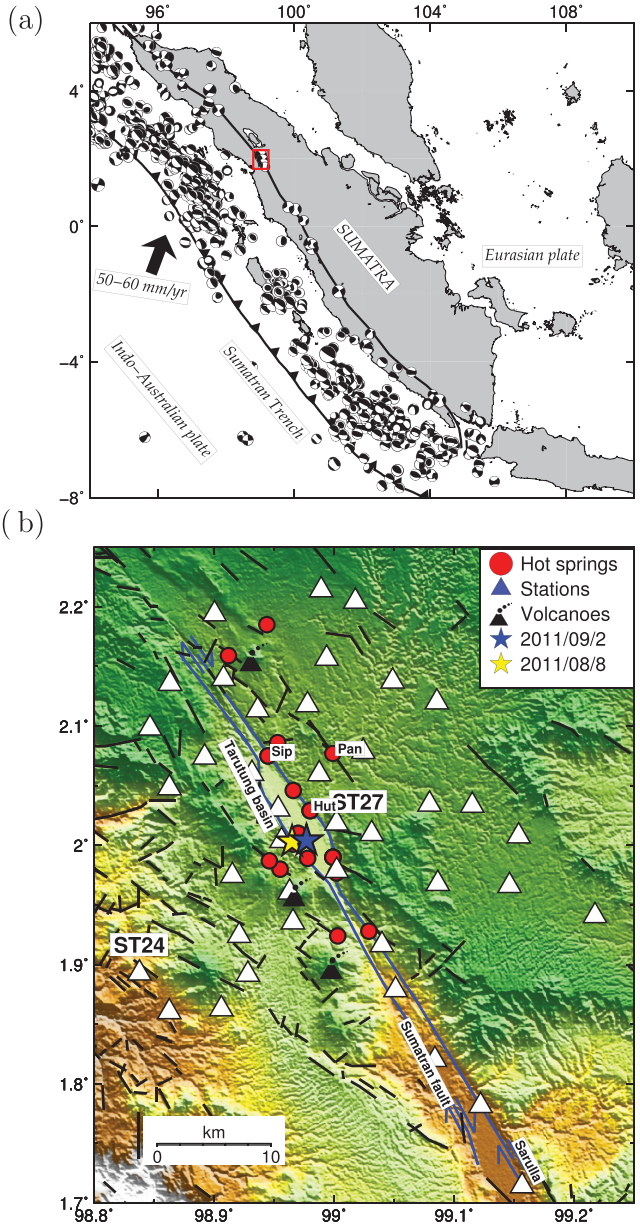

Figure 8. Regional geology map and location of the passive seismic experiment. (a) Regional geology map of Sumatra, Indonesia and (b) seismic network consists of 42 seismometers (white triangles) deployed in the Tarutung region. Tarutung region is represented by red box in (a). Lineaments (black lines), hot springs and the Sumatran fault trace (blue lines) inferred from satellite image are taken from Nukman & Moeck (2013). The seismic event occurred on 2011 August 8 and September 2 are indicated by the yellow and blue stars.

in the surroundings of the Tarutung depression (Fig. 8), covering an area of *ca.* 40 × 50 km^2. Only five seismometers could be installed along the Sumatran Fault (SF) traversing the Sarulla basin.

In this study, we select a subset of data which represents high precision seismic event locations, as they have been located using the multiple-event-determination method by making use of differential traveltime and cross-correlation waveform (Muksin *et al.* 2013). This subset of data consists of 357 seismic events. The corresponding waveforms of these seismic events are windowed seismograms with a length of 20 s starting around 5 s before the origin time, determined by the double-difference method. If the catalogue has

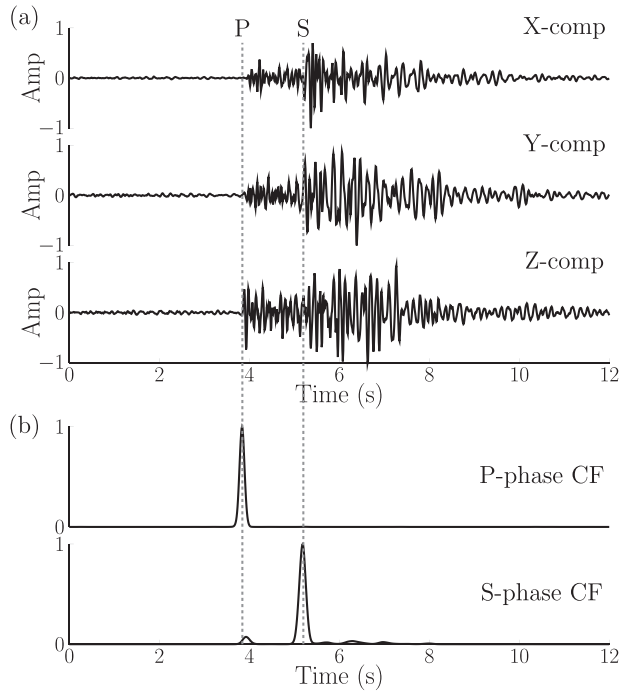

Figure 9. (a) Waveform of the three-component seismograms recorded at station S27 associated with the seismic event occurred on 2011 August 8 (see Fig. 8) filtered between 5 and 40 Hz, and (b) the *P*- and *S*-characteristic functions derived from mAIC and polarization attributes.

not yet been prepared for each event, the event triggering technique such as STA/LTA can also be used as a guide to determine the limit of the seismogram windowing. The purpose of the seismogram windowing is to speed up the processing time. Since a velocity sensor was used, we apply localization only to the velocity seismograms. By considering that most of the seismometers were installed near various public spots such as schools and offices, anthropogenic vibrations (or cultural noise) is likely to have contaminated the seismogram recordings as well as ambient natural noise. To reduce noise, the seismograms were filtered using a Butterworth bandpass with four poles and corner frequencies of 5 and 40 Hz.

Fig. 9 shows the *P*- and *S*-CFs computed from the corresponding three-component seismograms recorded at station ST27 associated with the seismic event occurred on 2011 August 8. The corresponding mAIC CFs and the largest eigenvalue have been shown in Figs 4(b) and (c). The window length of 0.4 s has been used. It can be seen that the spiky *P* and *S* CFs coincide with the onsets of *P* and *S* waves. The combination between the three-component mAIC CFs and polarization attributes (eq. 5) has shown its effectiveness to extract *S* waves. Furthermore, the multiplication between each component (eqs 6 and 8) improves the CF and removes artefacts of mAIC functions occurring outside the onsets of *S* and *P* waves.

The resulting *P* and *S* CFs then are used as the input to construct the image function. The traveltime database was generated by using the *P*- and *S*-velocity models obtained from previous traveltime tomography (Muksin *et al.* 2013). The amplitude stacking is performed within 0.4 s window length in equal weighting function. A window length of 0.4 s was applied in accordance with the window length used in the computation of the mAIC CF. The event location is estimated from the image function using the statistical approach (Anikiev *et al.* 2014). Fig. 10 presents the *P*-, *S*- and *PS*-image functions for the event shown in Fig. 8. The clearest maximum image value is shown by the *PS*-image function. However, the event locations resulting from the *P*-image function are closer to those resulted by the traveltime method where their absolute distances are 0.144, 0.107 and 0.26 km at WE, NS and depth axis, respectively. The estimated event locations at *S* and *PS* images are similar whose absolute distance with those resulted by the traveltime method, (0.394, 0.357 and 0.49 km) at WE, NS and depth axis, respectively. These results indicate that the *PS*-image function is dominated by the *S*-image function. This happens due to the fact that the *S*-image function has higher stacked amplitude than the *P*-image function. The higher stacked amplitude might be resulted from the better approximation of the stacking operator.

Fig. 11 shows the 357 seismic event locations resulting from diffraction stacking. At this figure, the locations resulting from the traveltime-based method are also shown (white circles). In general, the seismic event locations resulting from both methods are in a good agreement. The located seismic events are distributed along fault structures, near the hot springs. Most of the seismic events occurred around the western flank of the Sumatran Fault. The seismicity in the Tarutung basin shows a more complex pattern as it is distributed not only at the surface trace of the Sumatran Fault but also scattered across the Tarutung basin. At the southern part of this area, the located seismic events are more scattered. Moreover, the distance between those resulted by the diffraction stacking and traveltime methods is getting large particularly in depth axis due to a sparse coverage.

5 DISCUSSION AND CONCLUSIONS

We have evaluated an automated seismic event localization method that makes use a new CF based on the AIC function. As part of this evaluation, the event localization was applied to synthetic seismograms. The results show that the location of the sources was successfully recovered. The final image function is based on the largest eigenvalue of the covariance matrix between the *P*- and *S*-image functions. This approach provides a better focusing compared with the analysis of the original *P*- or *S*-image functions (Fig. 10) and gives an improved location of the seismic events.

Fig. 7 demonstrates that diffraction stacking of the CF provides much better results compared with the stacking of the actual waveforms. The poor performance (fuzzy image) from the stacking of the original waveforms is related with the undesired polarity variation effects from the source radiation pattern. These undesired effects can be avoided by use of the CF.

We then located 357 crustal earthquakes occurring around the Tarutung basin. The results are consistent with those derived by the traveltime-based method which is multiple-event determination with differential time (double difference, Fig. 11). A relatively small misfit occurs due to a dependency of the diffraction stacking to the discretization of the grid. The seismic event has to be located at the grid nodes. It is possible to improve the resolution of event location regardless the used grid spacing by determining the event location using a statistical approach (Anikiev *et al.* 2014). However, in case of complex image functions, that is, multiple amplitude buildup, this approach might lead to wrong locations.

The diffraction stacking, unlike the classical traveltime-based methods, can be conducted without the need of traveltime picks. Hence, this method does not require manually hand-picking which seems to be subjective. Moreover, a lot of time and efforts spent for manual traveltime picks can be saved. It is obvious that the

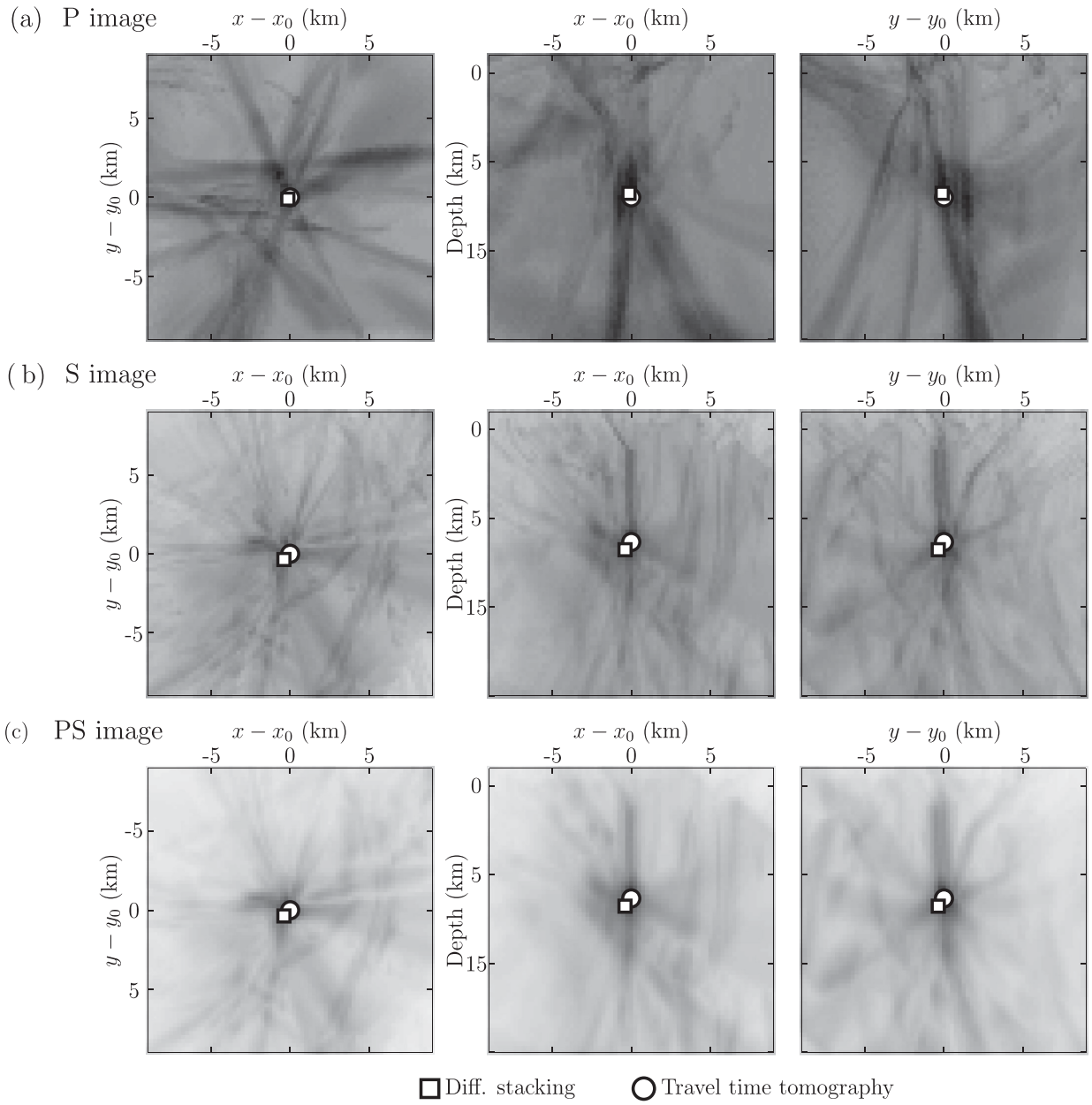

Figure 10. *P*-, *S*- and *PS*-image function related to the seismic event occurred on 2011 August 8 indicated by the yellow star in Fig. 8. The (x_0, y_0, z_0) is the location of seismic event estimated by the diffraction stacking method. The coordinates of seismic event (x_0, y_0, z_0) estimated by the diffraction stacking are (496.250, 221.5, 7.0), (496.5, 221.75, 6.25) and (496.5, 221.75, 6.25) in (a) *P*, (b) *S* and (c) *PS* images, respectively. Whereas that calculated by the traveltime is (496.106, 221.393, 6.740). Hence, their deviations between are 0.316, 0.723 and 0.723 km in *P*, *S* and *PS* images, respectively.

diffraction stacking involves an intensive computation particularly to compute the amplitude stacking at each grid. However, this aspect can be managed by some techniques, for example by implementing multistage processing. At the beginning a coarser discretization is applied. The next step is to find a more accurate result by refining the grid size and making use a resulted image function to limit the search area.

The comparison of the located seismic event resulting from the diffraction stacking and those resulting from classical traveltime method was made in order to demonstrate that the results of the diffraction stacking method is reliable. The classical method is not only picking the *P* and *S* arrivals, but normally also include (i) preparation of preliminary earthquake catalogue, (ii) earthquake relocation 1-D inversion and (iii) final earthquake relocation by using double difference method. This procedure is described in Muksin *et al.* (2013).

ACKNOWLEDGEMENTS

The first author is grateful to the financial support by the Ministry of Research, Technology and Higher Education of the Republic of Indonesia. Data were collected within the project 'Sustainability concepts for exploitation of geothermal reservoirs in Indonesia' funded by the German Federal Ministry of Education and Research (grant number 03G0753A). Seismic instruments were provided by

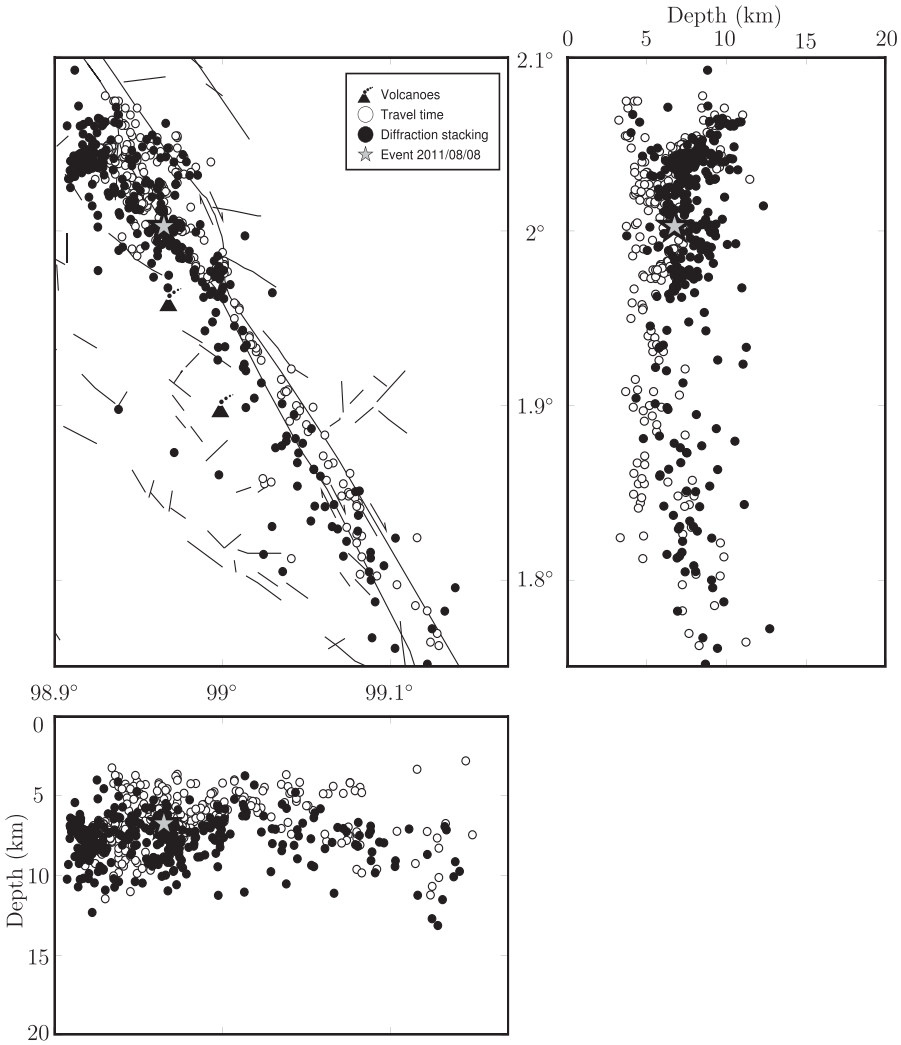

Figure 11. Distribution of seismic event locations at the Tarutung region derived from the diffraction stacking (black dots) and classical traveltime (circles) methods. The seismic event occurred on 2011 August 8 (Figs 9 and 10) is indicated by the grey star.

the Geophysical Instrument Pool Potsdam. Figures were produced using the Generic Mapping Tools (Wessel *et al.* 2013). The suggestions of the reviewers to improve the manuscript are gratefully acknowledged.

REFERENCES

Anikiev, D., Valenta, J., Staněk, F. & Eisner, L., 2014. Joint location and source mechanism inversion of microseismic events: benchmarking on seismicity induced by hydraulic fracturing, *Geophys. J. Int.,* **198,** 249–258.

Claerbout, J. & Fomel, S., 2014. *Geophysical Image Estimation by Example,* Stanford University.

Gajewski, D. J., Anikiev, D., Kashtan, B., Tessmer, E. & Vanelle, C., 2007. Source location by diffraction stacking, in *69th Annual International Meeting*, EAGE, Expanded Abstracts, EAGE.

Gharti, H.N., Oye, V., Roth, M. & Kühn, D., 2010. Automated microearthquake location using envelope stacking and robust global optimization, *Geophysics,* **75,** M27–M46.

Grigoli, F., Cesca, S., Vassallo, M. & Dahm, T., 2013. Automated seismic event location by travel-time stacking: an application to mining induced seismicity, *Seismol. Res. Lett.,* **84**(4), 666–677.

Grigoli, F., Cesca, S., Amoroso, O., Emolo, A., Zollo, A. & Dahm, T., 2014. Automated seismic event location by waveform coherence analysis, *Geophys. J. Int.,* **196,** 1742–1753.

Hansen, S.M. & Schmandt, B., 2015. Automated detection and location of microseismicity at Mount St. Helens with a large-N geophone array, *Geophys. Res. Lett.,* **42,** 7390–7397.

Jousset, P., Haberland, C., Bauer, K. & Arnason, K., 2011. Hengill geothermal volcanic complex (Iceland) characterized by integrated geophysical observations, *Geothermics,* **40,** 1–24.

Julian, B.R., 1983. Evidence for dyke intrusion earthquake mechanisms near long valley caldera, California, *Nature,* **303,** 323–325.

Kao, H. & Shan, S.-J., 2007. Rapid identification of earthquake rupture plane using source-scanning algorithm, *Geophys. J. Int.,* **168,** 1011–1020.

Langet, N., Maggi, A., Michelini, A. & Brenguier, F., 2014. Continuous kurtosis-based migration for seismic event detection and location, with application to Piton de la Fournaise volcano, La Réunion, *Bull. seism. Soc. Am.,* **104**(1), 229–246.

Maeda, N., 1985. A method for reading and checking phase times in autoprocessing system of seismic wave data, *Jishin,* **38,** 365–379.

Muksin, U., Bauer, K. & Haberland, C., 2013. Seismic Vp and Vp/Vs structure of the geothermal area around tarutung (North Sumatra, Indonesia) derived from local earthquake tomography, *J. Volc. Geotherm. Res.,* **260,** 27–42.

Nukman, M. & Moeck, I., 2013. Structural controls on a geothermal system in the Tarutung basin, North Central Sumatra, *J. Asian Earth Sci.,* **74,** 86–96.

Pesicek, J.D., Child, D., Artman, B. & Cieślik, K., 2014. Picking versus stacking in a modern microearthquake location: comparison of results from a surface passive seismic monitoring array in Oklahoma, *Geophysics,* **79,** KS61–KS68.

Staněk, F., Anikiev, D., Valenta, J. & Eisner, L., 2015. Semblance for microseismic event detection, *Geophys. J. Int.,* **201,** 1362–1369.

Tromp, J., Komatitsch, D. & Liu, Q., 2008. Spectral-element and adjoint methods in seismology, *Commun. Comput. Phys.,* **3,** 1–32.

Vavryčuk, V., 2015. Moment tensor decompositions revisited, *J. Seismol,* **19,** 231–252.

Wessel, P., Smith, W.H.F., Scharroo, R., Luis, J. & Wobbe, F., 2013. Generic Mapping Tools: improved version released, *EOS, Trans. Am. geophys. Un.,* **94,** 409–420.

Withers, M., Aster, R., Young, C., Beiriger, J., Harris, M., Moore, S. & Trujillo, J., 1998. A comparison of select trigger algorithms for automated global seismic phase and event detection, *Bull. seism. Soc. Am.,* **88,** 95–106.

Zhebel, O., 2013. Imaging of seismic event. The role of imaging conditions, acquisition geometry and source mechanisms, *PhD thesis,* University of Hamburg.